Holey Substrate-Directed Strain Patterning in Bilayer MoS_2

Yichao Zhang[1], Moon-Ki Choi[2], Greg Haugstad[3], Ellad B. Tadmor[2], and David J. Flannigan[1]*

[1]*Department of Chemical Engineering and Materials Science, University of Minnesota, 421 Washington Avenue SE, Minneapolis, MN 55455, USA*

[2]*Department of Aerospace Engineering and Mechanics, University of Minnesota, 110 Union Street SE, Minneapolis, MN 55455, USA*

[3]*Characterization Facility, University of Minnesota, 100 Union Street SE, Minneapolis, MN 55455, USA*

Abstract: Key properties of two-dimensional (2D) layered materials are highly strain tunable, arising from bond modulation and associated reconfiguration of the energy bands around the Fermi level. Approaches to locally controlling and patterning strain have included both active and passive elastic deformation *via* sustained loading and templating with nanostructures. Here, by float-capturing ultrathin flakes of single-crystal 2*H*-MoS_2 on amorphous holey silicon nitride substrates, we find that highly symmetric, high-fidelity strain patterns are formed. The hexagonally arranged holes and surface topography combine to generate highly conformal flake-substrate coverage creating patterns that match optimal centroidal Voronoi tessellation in 2D Euclidean space. Using TEM imaging and diffraction, as well as AFM topographic mapping, we determine that the substrate-driven 3D geometry of the flakes over the holes consists of symmetric, out-of-plane bowl-like deformation of up to 35 nm, with in-plane, isotropic tensile strains of up to 1.8% (measured with both selected-area diffraction and AFM). Atomistic and image simulations accurately predict spontaneous formation of the strain patterns, with van der Waals forces and substrate topography as the input parameters. These results show that predictable patterns and 3D topography can be spontaneously induced in 2D materials captured on bare, holey substrates. The method also enables electron scattering studies of precisely aligned, substrate-free strained regions in transmission mode.

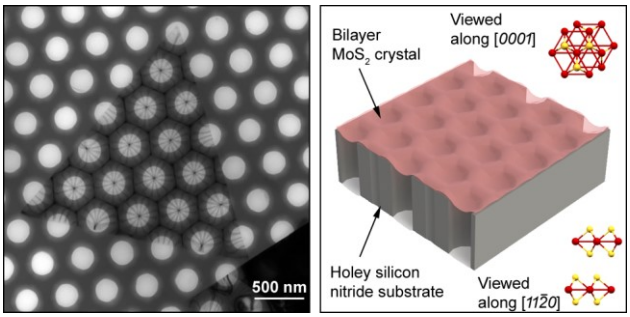

TOC Graphic

Keywords: suspended monolayers, 2D materials, TMD, TEM, AFM, atomistic simulations

The large elastic strains that can be endured by few- to monolayer 2D materials have drawn interest for flexible, strain-tunable optical and electronic applications.[1-6] Indeed, a number of methods employing a variety of engineering approaches and physical phenomena have been developed for inducing and controlling both local and whole-flake strain in ultrathin crystals of layered materials.[4,5,7-12] For heterogeneous and designed strain patterning, a variety of substrate and nano/microstructure templating methods have been developed, with which local periodic flake deformations are generated. In this way, one can pattern and control modulated optical and electronic properties, band-gap gradients, and periodic potential surfaces acting as single quantum emitters, crystal/plasmonic heterostructures, and artificial-atom crystals and exciton condensers.[13-23] Such methods are attractive, as they do not require constant and active application of an external load in order to maintain the deformed state, and they enable highly-controlled, localized heterogeneous strain conditions.

For substrates with patterned arrays of holes, as have been used for probe-tip measurements, pressure-driven deformation of few- to monolayer flakes, and ultrafast studies of exciton dynamics,[1,9,24-26] a strained configuration should form in the flake over the holes upon conformal coverage of a non-flat substrate topography. For a spatially-undulating topography with regular periodicity, the substrate template would thus generate a periodic, symmetric repeating strain pattern in the flake consisting of stable, localized deformation states that mimic the potential energy surface of an ordered array of atoms in a 2D crystal. Such an approach would have advantages over those employing flat, continuous substrates or those requiring constant application of an external load, as unimpeded scattering measurements of the resulting strain and its effects could be conducted in a transmission geometry.[7,10,25] Accordingly, here we employ a common transmission electron microscopy (TEM) specimen-prep method of crystal

float-capture onto bare, commercially available holey amorphous silicon nitride substrates for the spontaneous generation of stable, highly symmetric, high-fidelity strain patterns in bilayer and few-layer single-crystal 2*H*-MoS_2 flakes (simply MoS_2 from here forward). Again, while placement of few- to monolayer flakes of 2D materials over substrates with arrays of holes has been done,[1,9,24-26] the formation of surface tessellation strain patterns from holey substrates with regularly undulating surface topography has not yet been reported. Using TEM imaging and diffraction, atomic force microscopy (AFM) topographical mapping, and atomistic and image simulations, we show that strain-pattern formation indeed arises from conformal coverage of the underlying holey substrate. Using the same methods, we quantify both the nature and the magnitude of the strained regions over the holes, and we find that the periodic strain condition is isotropic in the *ab* plane and quantitatively consistent within individual flakes.

Results and Discussion

Figure 1 shows the TEM bright-field (BF) contrast patterns formed in bilayer single-crystal flakes of MoS_2 floated onto bare, holey amorphous silicon nitride substrates (see the Materials and Methods and Supporting Information for details; Figure S1 summarizes the TEM method used to determine the number of layers). The surface of these substrates (Ted Pella, 21586-10) is not flat but instead consists of a periodic, undulating topography with regions between the holes reaching a height maximum before sloping downward into the hole (*e.g.*, see Figures 1e, 3c, 5b, and S8). Further, the hole edges are not abrupt but instead gradually slope downward upon moving toward the hole center (Figs. 5b and S8). As can be seen in Figure 1a, the BF patterns consist of 2D arrays of close-packed hexagonal strong-contrast features, which we call "cells". For complete hexagonal cells (*i.e.*, cells with all six sides), 12-fold azimuthally

symmetric diffraction contrast bend-contour patterns radiate outward from the approximate center (*i.e.*, the hub) of each hole in a spoke-like fashion. The contrast patterns arise from a corresponding symmetric real-space distortion of the MoS_2 flake such that gradual bending in the crystal spatially modulates the Bragg-scattering condition. For BF imaging this produces regions of strong scattering called bend contours, where the Bragg condition is satisfied and the image counts are low (*i.e.*, a dark region in the image).[27] This is further described below and in the Supporting Information.

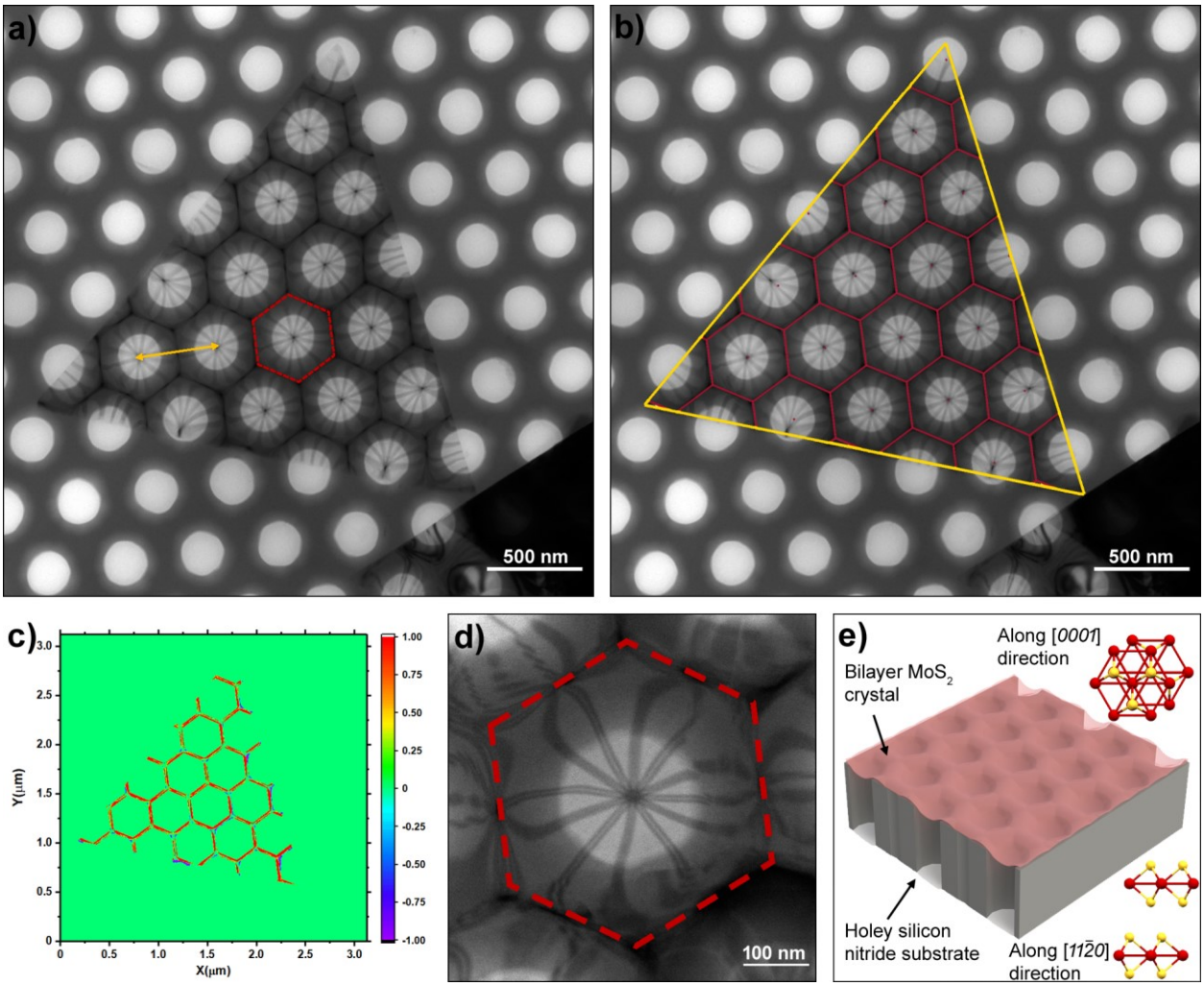

Figure 1. Diffraction contrast pattern in bilayer MoS_2 on a holey silicon nitride substrate. (a) TEM bright-field (BF) image of a bilayer MoS_2 single-crystal flake viewed along the [*0001*] direction displaying highly symmetric hexagonal diffraction contrast. The dashed red hexagon outlines a single cell, while the yellow double-headed arrow marks the separation between two adjacent cell center points. (b) Calculated Voronoi diagram (red) overlaid onto the observed pattern. Red dots mark the centers of the substrate holes determined using circular Hough transforms (see the Supporting Information). The yellow triangle highlights the flake edges. (c) Correlation color map of the calculated Voronoi diagram and the experimental pattern. The color bar denotes the correlation coefficient, with red being a perfect correlation of 1.00. (d) Magnified view of one cell with the approximate edges outlined in red. (e) Cross-sectional 3D schematic view of the flake and substrate showing conformal deformation of the MoS_2 bilayer. Representative lattice configurations for views along the layer stacking direction and parallel to the basal planes are also shown for reference.

We first consider the hexagonal contrast cells before discussing the spoke-like zone-axis pattern (ZAP) and then the associated flake deformation and strain. The hexagonal contrast patterns resemble a tessellated surface correlated with the patterned hole array. To demonstrate this, we used circular Hough transforms to find the geometric center of each hole (to avoid introducing experimenter bias) and then generated an optimal 2D centroidal Voronoi diagram that we then compared to the hexagonal contrast pattern in the TEM image (Fig. 1b,c) (see also the Supporting Information and Figure S2). The strong positive correlation between the experimental and calculated pattern confirms that the substrate hole configuration is at least partly responsible for the observed contrast pattern. That is, the number of sites (holes) covered

by the flake match the number of observed hexagonal contrast cells. Further, the cell size is dependent upon the overall site density, and the average pitch of the holes (406 ± 4 nm) agrees with the average distance between neighboring sites (410 ± 6 nm).

While the hexagonal arrangement of the substrate holes and the formation of hexagonally close-packed diffraction contrast patterns are clearly connected, the ZAP and the associated flake deformation are not completely described by tessellation alone. Importantly, the ZAP is a direct indicator of the degree of flake deformation over the hole, and therefore the flake strain, that is driven by the substrate topography. Before discussing this, we briefly note two other features in the BF images. First, magnified views reveal the relationship of the sides of the cells to the ZAPs (Fig. 1d). Bend contours radiating outward from the hub change direction and converge to form the hexagon sides upon approaching the cell boundary. This arises from the non-flat topography of the substrate (*e.g.*, see Figure S8), as shown schematically in Figure 1e. Second, the sides of incomplete cells around the flake edges do not deviate from the overall hexagonal pattern; note the strong positive correlation of these regions in Figure 1c. However, bend contours defining these cells do not all originate from the corresponding center point determined with the circular Hough transform, and the azimuthal symmetry of the ZAP is reduced. This suggests all regions of the flake that are in physical contact with the substrate are conforming, regardless of proximity to the crystal edges.

To better understand flake orientation and deformation, the ZAP within an individual cell was indexed using dark-field (DF) imaging (Fig. 2). The selected-area electron-diffraction (SAED) pattern obtained from a flake region over a substrate hole is indicative of orientation generally along the crystallographic [*0001*] direction (Fig. 2c). With DF imaging, the ZAP was indexed to the lowest-order Bragg reflections (Fig. 2b). Upon inspection of the characteristics of

the ZAP, it can be seen that the $\{10\bar{1}0\}$ planes produce uniform-intensity bend contours in real space, while the $\{11\bar{2}0\}$ planes produce a dark-light-dark pattern across the width of each contour (Fig. 2a,b; see also Fig. 1d). The dark-light-dark pattern results from *hkil* Friedel pairs of Bragg reflections (*e.g.*, $11\bar{2}0$ and $\bar{1}\bar{1}20$),[28] while the uniform-intensity contours associated with first-order reflections have relatively slightly broadened relrods.[27] Thus, the overall appearance of the ZAP is indicative of a symmetric out-of-plane deformation over the holes, with the relative relrod positions with respect to the Ewald sphere being responsible for the fine contrast structure of the contours.

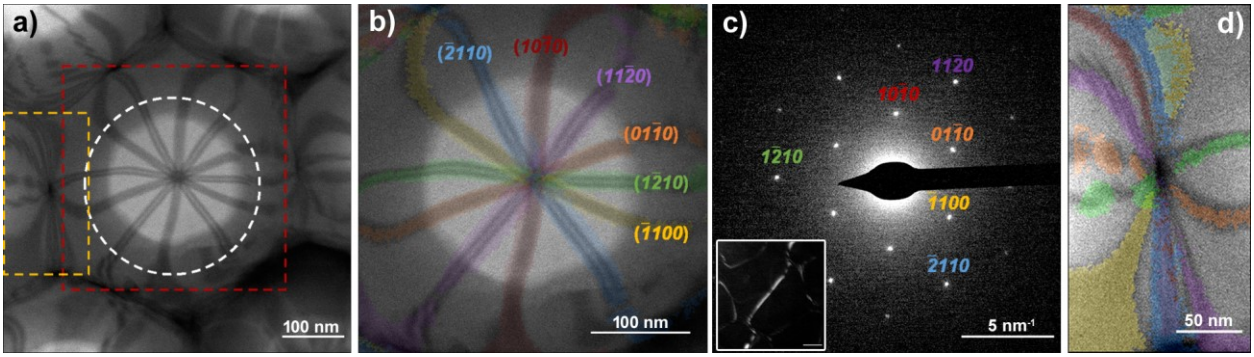

Figure 2. Indexing of the ZAP forming a single hexagonal cell. (a) BF image of one cell. Select regions of interest (ROIs) are highlighted (dashed red square for panel b and dashed yellow rectangle for panel d). The dashed white circle marks the selected area from which diffracted beam intensity was collected (panel c). (b) ZAP indexed using SAED and DF imaging. False coloring corresponds to the indexed Bragg reflections in panel c. (c) Partially indexed SAED pattern from the selected area in panel a. Inset is a representative DF image of the $(11\bar{2}0)$ bend contour. Inset scale bar = 100 nm. (d) Magnified BF image of the ROI highlighted with the dashed yellow rectangle in panel a. False coloring corresponds to that in panels b and c.

In order to characterize and quantify the topography of the flakes over the holes, bend-contour behavior with specimen tilt angle (α) was tracked (Fig. 3a,b). This was complemented with AFM topographic mapping of a few-layer flake (Fig. 3c,d). Tilting along a single axis orthogonal to the approximate [*0001*] zone-axis direction ($\alpha = 0°$) causes the ZAP center position (*i.e.*, the "hub") to translate along a line passing through the center position (Fig. 3a, yellow and red circles, respectively; see Supporting Video 1). The spoke-like ZAP regions also respond to tilting by curving in the same direction as movement of the hub; *e.g.*, the ends of the spokes curve to the right when the hub moves to the right. This behavior is further indication of symmetric flake curvature over the holes and can be used to quantify the out-of-plane bending. To do so, an analytical model was used that approximates the flake curvature as an arc (see the Supporting Information and Figure S3). In this way, the α-dependent hub displacement (x_c) from the center position behaves following Equation 1.

$$x_c(\alpha) = \frac{1}{2}\left(\frac{a^2}{b} - b\right)\sin\alpha \qquad (1)$$

Here, a is half the substrate hole pitch, and b is the flake bending height (*i.e.*, the out-of-plane deformation). A plot of measured x_c at various α positions is approximately linear for a fixed value of a at small α, with the slope directly determined by b (Fig. S4). Here, least-squares linear fits to measurements from four different cells returned an average flake bending height of 31.4 nm (Fig. 3b and Fig. S5). These measurements were compared to AFM measurements of surface topography of the same MoS_2 flake (Fig. 3c,d) (see the Materials and Methods for details). An average peak-to-valley difference of 34.6 nm was determined from profiles along two different directions, in good agreement with the tilt experiments. Further, the lateral positions of the flake valleys occur at the centers of the underlying substrate holes, showing that the flake is deformed inward like a bowl into the substrate holes rather than outward like a dome

(also see Fig. S8c). This further indicates that the flakes conform to the underlying substrate, illustrating a high-fidelity templating effect.

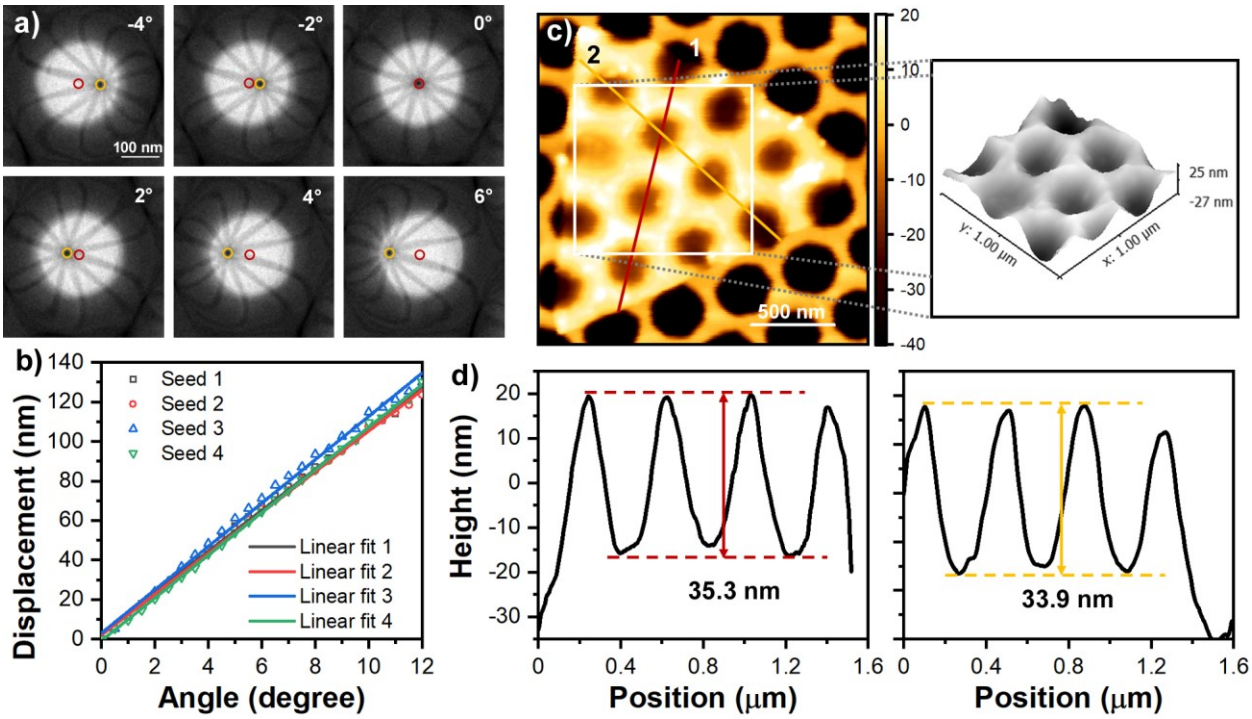

Figure 3. Flake bending-height determination using BF imaging of specimen tilting and AFM topographic mapping. (a) Representative BF images of a single cell at various α-tilt angles. Red and yellow circles mark the center and ZAP hub positions, respectively. Spacing between the positions is x_c. (b) x_c *vs.* α-tilt angle for four different cells. Least-squares linear fits to each set of data are shown. The slopes were used to calculate b using Equation 1. (c) AFM height map of the same flake shown in panel a. Units of the color bar are nm. The rendering to the right shows the 3D topography of the region outlined in white. (d) Height profiles along lines 1 (left) and 2 (right) in panel c passing through the centers of the substrate holes. From these, the maximum height modulation of the flake was measured to be 35.3 nm and 33.9 nm for lines 1

and 2, respectively. See Figure S8 for additional height maps and true vertical-to-lateral aspect ratio profiles of the flake and the bare substrate.

Average strain of the flakes over the substrate holes was measured with SAED and further estimated with AFM topographic measurements and a simple geometric model. With SAED, a selected-area aperture was used to isolate diffraction signal from an approximately 200-nm diameter central region of the flake over a hole (Fig. 4a,b). Accordingly, average basal-plane strain along a particular crystallographic direction was determined by comparing the measured reciprocal-space distance (d^{-1}) between Friedel pairs to the theoretical distance for the fully-relaxed 2*H*-MoS_2 structure (Fig. 4b,c).[29] This method has also been used to measure strain in WSe_2 films grown directly on thin SiO_2 membranes.[10] Here, the experimental distance between the $10\bar{1}0$ and $\bar{1}010$ pair was 7.16 nm^{-1}, compared to the theoretical fully relaxed distance of 7.30 nm^{-1}. This translates into an average real-space tensile strain of 1.7 ± 0.2%. Ten separate measurements from three different flakes returned tensile strains ranging from 0.8 to 1.8%, which also was found to be isotropic with respect to the basal plane (*i.e.*, spacing between all Friedel pairs was uniformly decreased relative to the relaxed structure). Note that, while strains varied from flake to flake, regions within individual flakes showed the same amount of strain across multiple individual cells (see Table S2 in the Supporting Information). Average tensile strains of 1.5 ± 0.2% were also estimated from AFM measurements of the crystal height profile and the hole size, in good agreement with the SAED measurements (error propagated from the profile errors; see the Supporting Information and Figure S6 for descriptions of the geometric model). At the atomic scale, this degree of strain causes an average increase of Δd_1 = 5.8 pm in the Mo-Mo real-space distance along the [$11\bar{2}0$] direction and an average increase of Δd_2 = 1.5

pm in the Mo-S distance along the [$10\bar{1}0$] direction when projected onto the plane of Mo atoms (Fig. 4c).[30-32] See the Supporting Information and Figure S7 for additional descriptions of the SAED calibration.

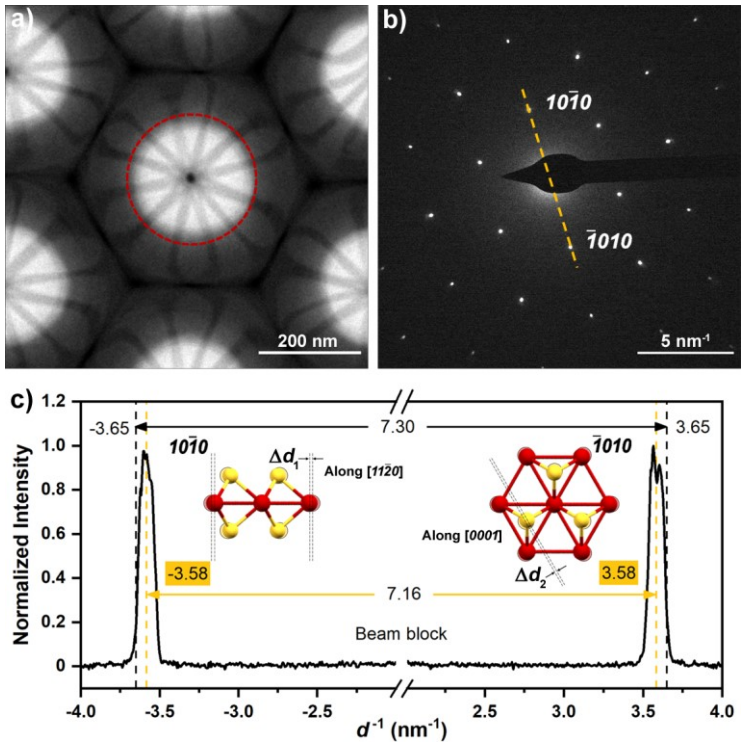

Figure 4. Average basal-plane strain of flake regions over substrate holes measured with SAED. (a) BF image of the same few-layer MoS_2 specimen as in Figure 3. The dashed red circle marks the region from which diffraction signal was obtained. (b) SAED pattern from the region in panel a, with a Friedel pair indexed. (c) Normalized intensity profile of the dashed yellow line in panel b. Dashed yellow vertical lines mark the experimentally observed positions of the $10\bar{1}0$ and $\bar{1}010$ Bragg spots (d^{-1} = -3.58 nm^{-1} and 3.58 nm^{-1}, respectively), while dashed black vertical lines mark the theoretical positions for the fully relaxed structure (±3.65 nm^{-1}). The insets illustrate the associated atomic-scale distortions of Δd_1 = 5.8 pm and Δd_2 = 1.5 pm, as viewed along the [$11\bar{2}0$] and [0001] real-space crystallographic directions, respectively.

The molecular-level nature of the substrate-directed elastic deformation and strain patterning was further elucidated using atomistic simulations (Fig. 5a,b). Energy minimization using a reactive bond order (REBO) potential for intralayer interactions and a Lennard-Jones potential for van der Waals interlayer interactions was performed to determine the equilibrium structure of bilayer MoS_2 suspended over an amorphous silicon nitride substrate with a hexagonal array of holes and with topography determined with AFM (Fig. 5b inset and Fig. S8). Calculations were performed on arrays consisting of holes with radii of 5, 10, and 20 nm and pitch sizes of 20, 40, and 80 nm (center-to-center distance) (see the Materials and Methods section and the Supporting Information for details). The reduced dimensions compared to the experiments were necessitated by computing time; the trends observed indicate the results at smaller dimensions extrapolate to the larger experimental scale. For a bare substrate, regions between the holes were relatively flat halfway between neighboring holes, with a decrease in height upon approaching the hole edge. A compressive pre-strain of 1.6% was applied to the bilayer and was needed to match the experimental TEM contrast patterns and the magnitude of the observed deformation. One possible source for this pre-strain is polymer shrinkage during the specimen transfer process, though we are not certain of the exact origin.[33]

After energy minimization, the MoS_2 bilayer flake conforms to the shape of the underlying substrate *via* van der Waals forces. Further, the flakes experience a downward deflection into the hole due to localized moments at the hole edges, as experimentally observed. The in-plane tensile strain in the freestanding flake region then results from the out-of-plane bowl-like bending and a periodicity constraint on the length. As with the hexagonal cells in the TEM images, this leads to formation of hexagonal borders in the flake between neighboring

holes. Further, the shape smoothly changes to a symmetric bowl as it approaches the hole center due to the absence of substrate-flake interactions and the large ratio of lateral dimension to out-of-plane deflection, again consistent with experiment. This behavior was observed for all simulated hole sizes. Bending heights of 1.6, 2.6, and 5.6 nm resulted for the 5-, 10-, and 20-nm hole radii, respectively, thus displaying a dependence upon the size of the system (as noted above), with larger heights resulting from larger holes. By noting the ratio of the simulated bending height to the hole radius (0.29 ± 0.03), the bending height for a 100-nm radius hole (same as experiment) is predicted to be 29 nm, in good agreement with that measured with SAED and AFM. Note that the magnitude of the phenomenological compressive pre-strain also impacts the curvature of the bilayer, with larger values causing larger bending heights.

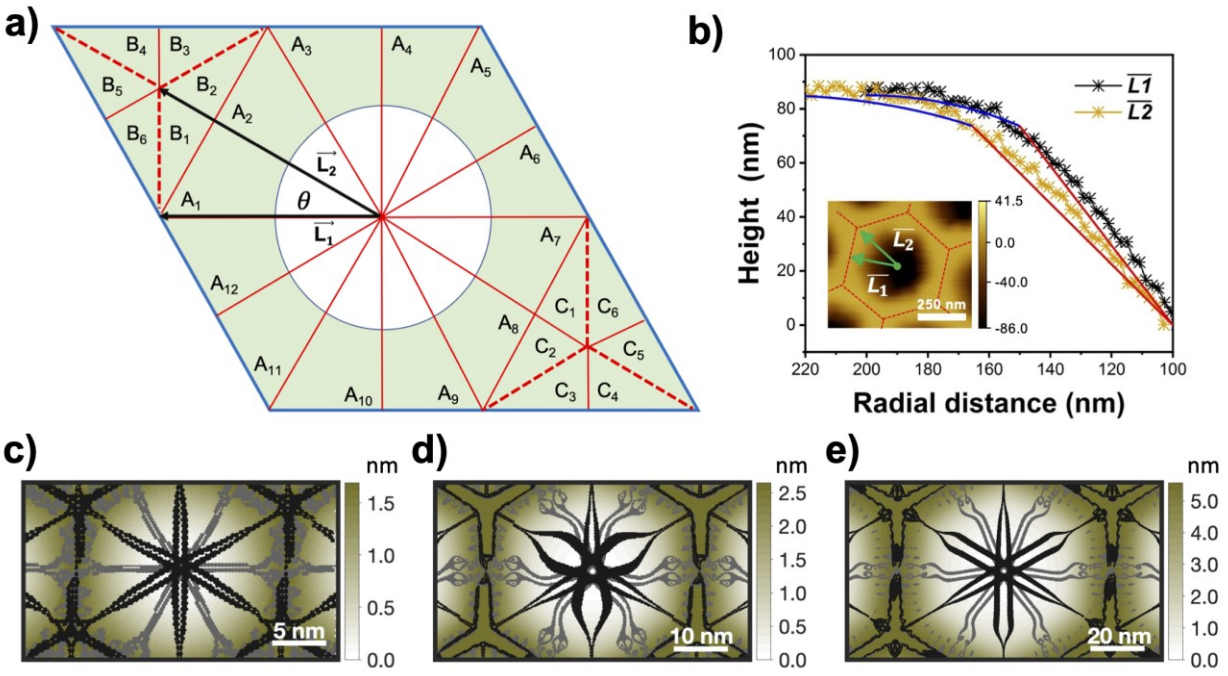

Figure 5. Atomistic simulation of bilayer MoS_2 on an amorphous holey silicon nitride substrate. (a) Parallelogram unit cell (outlined in blue) of the simulation and the geometry of the substrate.

The light green region represents the substrate, and the white region represents the hole. The red dashed lines mark the tessellation cell boundaries. The thin red lines divide the substrate unit cell into sub-regions A, B, and C displaying mirror symmetry, with two representative directions, $\overrightarrow{L_1}$ and $\overrightarrow{L_2}$, and the angle θ = 30° between them labeled. (See the Supporting Information for details on how the indicated symmetries are used in the computation of the interlayer interactions between the MoS_2 flake and the substrate.) (b) Bare-substrate AFM height profiles along the $\overrightarrow{L_1}$ and $\overrightarrow{L_2}$ directions shown in the inset, overlaid on the topographic map. Ellipse (red) and linear (blue) equations are adopted to fit the experimental height profiles. The red dashed lines on the AFM image in the inset mark the substrate peak-height positions. Height color bar on the inset is in units of nanometers. (c)-(e) Simulated height maps of a bilayer MoS_2 flake on a holey substrate matching the experimental topography. Hole radii are 5, 10, and 20 nm from left to right. Simulated bend contours of the $\{10\bar{1}0\}$ (black) and $\{11\bar{2}0\}$ (grey) families of planes are overlaid on the height maps.

Finally, to relate the calculated substrate-driven elastic deformation and strain patterning to the diffraction contrast patterns in the TEM images, a bend-contour simulation was performed using the minimized atomic structure (see the Supporting Information for details) (Fig. 5c-e). Bend contours from the $\{10\bar{1}0\}$ and $\{11\bar{2}0\}$ planes were simulated in order to compare with the experiments (see Fig. 2). The results show hexagonally close-packed cells and 12-fold azimuthally symmetric contrast features over the holes that comprise the cell sides, matching experiments. More specifically, the simulated bend contours pass the center point of the hole and are mostly linear within the cell boundaries. As the bend contours approach the cell sides, the features become distorted and eventually comprise the hexagons. This further illustrates that

conformal coverage of the substrate by the flake and the bowl-like deformation and resulting in-plane tensile strain produces highly symmetric, spatially repeating elastic deformation over both the hole and the solid substrate regions.

Summary and Conclusions

We report a simple method for the patterning of strain in flakes of 2D materials, specifically the formation of tessellation patterns in bilayer and few-layer flakes of MoS_2 float-captured on bare, amorphous, holey silicon nitride substrates with regularly undulating surface topography. We find that pattern formation is driven by weak-force interactions between the MoS_2 crystal and the underlying substrate, specifically both the hexagonal array of holes and the substrate surface topography. Diffraction-contrast patterns in the bright-field TEM images follow the most efficient packing pathway for a 2D geometry in Euclidean space, thus being amenable to quantitative prediction for various template geometries and topographies. Using a combination of electron diffraction techniques supported with AFM topographical mapping, strain over the holes was found to be tensile in nature, isotropic, and highly symmetric and repeating, reaching nearly 2% in the freestanding regions. The experimental results – including flake topography and nature of the strain – were supported with atomistic and bend-contour simulations, which also revealed spatial scaling trends in addition to the 3D elastic deformations. The observations reported here provide a simple, straightforward means for patterning repeating, freestanding strained regions in 2D materials, with implications for both fundamental and applied studies of passive and active strain modulation in ultrathin layered materials.

METHODS

Electron and Atomic Force Microscopies. All BF, DF, and SAED experiments were conducted with an FEI Tecnai Femto TEM (Thermo Fisher Scientific) operated at 200 kV in thermionic mode and equipped with a Gatan OneView 16 MP CMOS camera. AFM imaging was performed using a Keysight 5500 scanning probe microscope operated in ambient air (RH 25%) running Picoview 1.20 software. The XYZ piezoscanner (model 9524B) was operated in closed loop *X*-*Y* with a *Z* range of 8 μm (spread over 2^{16} digitization). Data were collected in the dynamic mode, also referred to as AC mode, under conventional amplitude-modulation feedback, with cantilever vibrated at its fundamental flexural resonance frequency, to provide height and phase along with error signal (amplitude) images. Imaging scan rates were 0.5 lines per second at a resolution of 512 by 512 pixels. An uncoated rectangular silicon cantilever (AppNano model FORT) with integrated silicon tip (3-sided pyramidal terminated by high-aspect-ratio end; nominal radius of curvature 6 nm), spring constant 2 N/m, and measured resonance frequency of 67.32 kHz at 200 nm from tip-sample engagement was used for the reported measurements. By imaging across the edges of substrate holes (thereby reverse imaging the tip shape), we confirmed a tip-opening half angle of less than 10° near its high-aspect-ratio end, whereas the steepest topography analyzed in this work was approximately 30° from vertical. The cantilever was driven to produce a free oscillation amplitude of approximately 50 nm. The set point for feedback tracking of topography was regularly explored over a range of 70-90% of the free oscillation amplitude, yielding no detectable change in measured topography. Aided by the phase signal and amplitude and phase *vs. Z* curves, the aforementioned parameter setting ensured that the oscillator was maintained in the net attractive regime to achieve a delicate tip-sample interaction with negligible mechanical deformation (consistent with the observed set-point-independent topography).[34] Data post-processing was performed using the freeware

Gwyddion (v2.58). Masking was employed using *Z* thresholding so as to isolate a narrow *Z*-window of bare substrate surface between holes, such that these data could be fit with a second-order polynomial surface, which was then subtracted from an entire height image so as to remove scanner non-idealities (*e.g.*, *Z* scanner nonlinearity and *X*-*Y* scanner cross coupling).[34]

Specimen Preparation. MoS_2 specimens were prepared using adhesive tape and repeated exfoliation of a bulk crystal in the 2*H* phase (2D Semiconductors).[35-37] Exfoliated flakes were transferred onto an NaCl single crystal (Ted Pella) by rubbing the tape on the surface. Coverage and the presence of flakes was qualitatively checked with an optical stereo microscope (AmScope). The NaCl crystal and adhering flakes were washed repeatedly with isopropyl alcohol in order to remove residual adhesive, followed by drying in air. Next, 20.0 ± 0.4 μL of 4 wt% poly(methyl methacrylate) (PMMA) in anisole was drop-cast onto the NaCl surface with adhering MoS_2 flakes. The entire specimen was then annealed at 100 °C in air for 10 minutes, resulting in the formation of a self-supported matrix assembly. The matrix was then floated off the NaCl crystal in DI water and captured with a holey amorphous silicon nitride substrate (Ted Pella, 21586-10). The substrate-supported matrix assembly was washed repeatedly with acetone in order to remove the PMMA. Note that the generation of isolated single-crystal bilayer and few-layer flakes such as shown in Figure 1 is not as common as multi-layer, ill-defined flakes with high defect densities. The objective here was to report the observation and characterization of pattern formation in such flakes on holey substrates with non-flat topography and to emphasize the highly symmetric, repeating strain patterning that results. Extension to other deposition methods, such as CVD, and to scaling-up the approach require further study.

Atomistic and Bend-contour Simulations. Atomistic simulations were performed for a bilayer 2*H*-MoS_2 flake on an amorphous silicon nitride substrate containing a hexagonal pattern

of holes with radii of 5, 10, and 20 nm and with a pitch of 20, 40, and 80 nm, respectively. The surface topography characterized with AFM was also incorporated into the simulations. The simulations were performed using the LAMMPS molecular dynamics code.[38,39] The modeled configuration consisted of a parallelepiped-shaped periodic cell of bilayer MoS_2 consistent with one unit cell of the underlying substrate. The intralayer interactions in the bilayer were modeled using a reactive bond-order (REBO) potential.[40,41] Interlayer interactions between the crystal layers and between the bilayer and substrate were modeled using a Lennard-Jones potential. Equilibrium configurations were obtained by minimizing the total energy using a fast inertial relaxation engine (FIRE) algorithm available in LAMMPS.[42] Bend-contour simulations were performed using MATLAB. See the Supporting Information for additional details.

ASSOCIATED CONTENT

Supporting Information

The Supporting Information is available free of charge at (URL inserted by publisher).

Specimen thickness, simulated and experimentally observed Voronoi diagrams, crystal deformation height, estimation of strain from AFM measurements, SAED strain measurements, effects of specimen tilt on strain measurements, calibration of the SAED patterns, AFM topographic mapping of the flakes and the bare substrates, external energy from a holey substrate by tri-cubic interpolation, bend contour simulations (PDF)

Tilt series of an MoS_2 crystal on a holey silicon nitride substrate displaying tessellation patterns (AVI)

AUTHOR INFORMATION

Corresponding Author

David J. Flannigan

orcid.org/0000-0002-1829-1868

Email: flan0076@umn.edu

Authors

Yichao Zhang

orcid.org/0000-0003-1225-3278

Current address: Department of Materials Science and Engineering, University of Illinois at Urbana-Champaign, Urbana, Illinois 61801

Author Contributions

Y.Z. contributed to the formal analysis, investigation, methodology, software, validation, visualization, writing – original draft, and writing – review and editing. M.-K.C. contributed to the formal analysis, methodology, software, visualization, writing – original draft, and writing – review and editing. Y.Z. and M.-K.C. contributed equally to this work. G.H. contributed to the investigation, formal analysis, writing – original draft, and writing – review and editing. D.J.F. and E.B.T. contributed to the conceptualization, formal analysis, funding acquisition, methodology, project administration, resources, supervision, visualization, writing – original draft, and writing – review and editing. See the NISO CRediT taxonomy for definitions of contributor roles.

Notes

The authors declare no competing financial interest.

ACKNOWLEDGMENTS

This work was supported primarily by the National Science Foundation through the University of Minnesota MRSEC under Award Number DMR-2011401. This material is based upon work partially supported by the National Science Foundation under Grant No. DMR-1654318 and the Army Research Office (W911NF-14-1-0247) under the MURI program. Parts of this work were carried out in the Characterization Facility, University of Minnesota, which receives partial support from the NSF through the MRSEC (Award Number DMR-2011401) and the NNCI (Award Number ECCS-2025124) programs. E.B.T. and M.C. thank Jan Fransaer for helpful discussions on modeling MoS_2-substrate interactions. Y.Z. acknowledges support from the Louise T. Dosdall Fellowship.

REFERENCES

1. Bertolazzi, S.; Brivio, J.; Kis, A. Stretching and Breaking of Ultrathin MoS_2. *ACS Nano* **2011**, *5*, 9703-9709.

2. He, K.; Poole, C.; Shan, J.; Mak, K. F. Experimental Demonstration of Continuous Electronic Structure Tuning *via* Strain in Atomically Thin MoS_2. *Nano Lett.* **2013**, *13*, 2931-2936.

3. Conley, H. J.; Wang, B.; Ziegler, J. I.; Haglund, R. F.; Pantelides, S. T.; Bolotin, K. I. Bandgap Engineering of Strained Monolayer and Bilayer MoS_2. *Nano Lett.* **2013**, *13*, 3626-3630.

4. Shi, H.; Pan, H.; Zhang, Y.-W.; Yakobson, B. I. Quasiparticle Band Structures and Optical Properties of Strained Monolayer MoS_2 and WS_2. *Phys. Rev. B* **2013**, *87*, 155304.

5. Zhu, C. R.; Wang, G.; Liu, B. L.; Marie, X.; Qiao, X. F.; Zhang, X.; Wu, X. X.; Fan, H.; Tan, P. H.; Amand, T.; Urbaszek, B. Strain Tuning of Optical Emission Energy and Polarization in Monolayer and Bilayer MoS_2. *Phys. Rev. B* **2013**, *88*, 121301.

6. Castellanos-Gomez, A.; Roldán, R.; Cappelluti, E.; Buscema, M.; Guinea, F.; van Der Zant, H. S. J.; Steele, G. A. Local Strain Engineering in Atomically Thin MoS_2. *Nano Lett.* **2013**, *13*, 5361-5366.

7. Yang, S.; Wang, C.; Sahin, H.; Chen, H.; Li, Y.; Li, S.-S.; Suslu, A.; Peeters, F. M.; Liu, Q.; Li, J.; Tongay, S. Tuning the Optical, Magnetic, and Electrical Properties of $ReSe_2$ by Nanoscale Strain Engineering. *Nano Lett.* **2015**, *15*, 1660-1666.

8. Manzeli, S.; Allain, A.; Ghadimi, A.; Kis, A. Piezoresistivity and Strain-Induced Band Gap Tuning in Atomically Thin MoS_2. *Nano Lett.* **2015**, *15*, 5330-5335.

9. Lloyd, D.; Liu, X.; Christopher, J. W.; Cantley, L.; Wadehra, A.; Kim, B. L.; Goldberg, B. B.; Swan, A. K.; Bunch, J. S. Band Gap Engineering with Ultralarge Biaxial Strains in Suspended Monolayer MoS_2. *Nano Lett.* **2016**, *16*, 5836-5841.

10. Ahn, G. H.; Amani, M.; Rasool, H.; Lien, D.-H.; Mastandrea, J. P.; Ager Iii, J. W.; Dubey, M.; Chrzan, D. C.; Minor, A. M.; Javey, A. Strain-Engineered Growth of Two-Dimensional Materials. *Nat. Commun.* **2017**, *8*, 608.

11. Shao, Z.; Fu, Z.-G.; Li, S.; Cao, Y.; Bian, Q.; Sun, H.; Zhang, Z.; Gedeon, H.; Zhang, X.; Liu, L.; Cheng, Z.; Zheng, F.; Zhang, P.; Pan, M. Strongly Compressed Few-Layered $SnSe_2$ Films Grown on a $SrTiO_3$ Substrate: The Coexistence of Charge Ordering and Enhanced Interfacial Superconductivity. *Nano Lett.* **2019**, *19*, 5304-5312.

12. Tyurnina, A. V.; Bandurin, D. A.; Khestanova, E.; Kravets, V. G.; Koperski, M.; Guinea, F.; Grigorenko, A. N.; Geim, A. K.; Grigorieva, I. V. Strained Bubbles in van der Waals Heterostructures as Local Emitters of Photoluminescence with Adjustable Wavelength. *ACS Photonics* **2019**, *6*, 516-524.

13. Lee, J.-K.; Yamazaki, S.; Yun, H.; Park, J.; Kennedy, G. P.; Kim, G.-T.; Pietzsch, O.; Wiesendanger, R.; Lee, S.; Hong, S.; Dettlaff-Weglikowska, U.; Roth, S. Modification of Electrical Properties of Graphene by Substrate-Induced Nanomodulation. *Nano Lett.* **2013**, *13*, 3494-3500.

14. Reserbat-Plantey, A.; Kalita, D.; Han, Z.; Ferlazzo, L.; Autier-Laurent, S.; Komatsu, K.; Li, C.; Weil, R.; Ralko, A.; Marty, L.; Guéron, S.; Bendiab, N.; Bouchiat, H.; Bouchiat, V. Strain Superlattices and Macroscale Suspension of Graphene Induced by Corrugated Substrates. *Nano Lett.* **2014**, *14*, 5044-5051.

15. Gill, S. T.; Hinnefeld, J. H.; Zhu, S.; Swanson, W. J.; Li, T.; Mason, N. Mechanical Control of Graphene on Engineered Pyramidal Strain Arrays. *ACS Nano* **2015**, *9*, 5799-5806.

16. Li, H.; Contryman, A. W.; Qian, X.; Ardakani, S. M.; Gong, Y.; Wang, X.; Weisse, J. M.; Lee, C. H.; Zhao, J.; Ajayan, P. M.; Li, J.; Manoharan, H. C.; Zheng, X. Optoelectronic Crystal of Artificial Atoms in Strain-Textured Molybdenum Disulphide. *Nat. Commun.* **2015**, *6*, 7381.

17. Branny, A.; Kumar, S.; Proux, R.; Gerardot, B. D. Deterministic Strain-Induced Arrays of Quantum Emitters in a Two-Dimensional Semiconductor. *Nat. Commun.* **2017**, *8*, 15053.

18. Jiang, Y.; Mao, J.; Duan, J.; Lai, X.; Watanabe, K.; Taniguchi, T.; Andrei, E. Y. Visualizing Strain-Induced Pseudomagnetic Fields in Graphene through an hBN Magnifying Glass. *Nano Lett.* **2017**, *17*, 2839-2843.

19. Mangu, V. S.; Zamiri, M.; Brueck, S. R. J.; Cavallo, F. Strain Engineering, Efficient Excitonic Photoluminescence, and Exciton Funnelling in Unmodified MoS_2 Nanosheets. *Nanoscale* **2017**, *9*, 16602-16606.

20. Martella, C.; Mennucci, C.; Cinquanta, E.; Lamperti, A.; Cappelluti, E.; Buatier De Mongeot, F.; Molle, A. Anisotropic MoS_2 Nanosheets Grown on Self-Organized Nanopatterned Substrates. *Adv. Mater.* **2017**, *29*, 1605785.

21. Rahaman, M.; Rodriguez, R. D.; Plechinger, G.; Moras, S.; Schüller, C.; Korn, T.; Zahn, D. R. T. Highly Localized Strain in a MoS_2/Au Heterostructure Revealed by Tip-Enhanced Raman Spectroscopy. *Nano Lett.* **2017**, *17*, 6027-6033.

22. Hu, Y.; Zhang, F.; Titze, M.; Deng, B.; Li, H.; Cheng, G. J. Straining Effects in MoS_2 Monolayer on Nanostructured Substrates: Temperature-Dependent Photoluminescence and Exciton Dynamics. *Nanoscale* **2018**, *10*, 5717-5724.

23. Liu, B.; Liao, Q.; Zhang, X.; Du, J.; Ou, Y.; Xiao, J.; Kang, Z.; Zhang, Z.; Zhang, Y. Strain-Engineered van der Waals Interfaces of Mixed-Dimensional Heterostructure Arrays. *ACS Nano* **2019**, *13*, 9057-9066.

24. Lee, C.; Wei, X. D.; Kysar, J. W.; Hone, J. Measurement of the Elastic Properties and Intrinsic Strength of Monolayer Graphene. *Science* **2008**, *321*, 385-388.

25. Shi, H.; Yan, R.; Bertolazzi, S.; Brivio, J.; Gao, B.; Kis, A.; Jena, D.; Xing, H. G.; Huang, L. Exciton Dynamics in Suspended Monolayer and Few-Layer MoS_2 2D Crystals. *ACS Nano* **2013**, *7*, 1072-1080.

26. Liu, K.; Yan, Q.; Chen, M.; Fan, W.; Sun, Y.; Suh, J.; Fu, D.; Lee, S.; Zhou, J.; Tongay, S.; Ji, J.; Neaton, J. B.; Wu, J. Elastic Properties of Chemical-Vapor-Deposited Monolayer MoS_2, WS_2, and Their Bilayer Heterostructures. *Nano Lett.* **2014**, *14*, 5097-5103.

27. De Graef, M., *Introduction to Conventional Transmission Electron Microscopy*. Cambridge University Press: Cambridge, 2003.

28. Friedel, G. Sur les Symétries Cristallines que Peut Révéler la Diffraction des Rayons X. *C. R. Acad. Sci., Paris* **1913**, *157*, 1533-1536.

29. Schönfeld, B.; Huang, J. J.; Moss, S. C. Anisotropic Mean-Square Displacements (MSD) in Single Crystals of 2*H*- and 3*R*-MoS_2. *Acta Crystallogr., Sect. B: Struct. Sci.* **1983**, *39*, 404-407.

30. Byskov, L. S.; Nørskov, J. K.; Clausen, B. S.; Topsøe, H. DFT Calculations of Unpromoted and Promoted MoS_2-Based Hydrodesulfurization Catalysts. *J. Catal.* **1999**, *187*, 109-122.

31. Li, Y.; Zhou, Z.; Zhang, S.; Chen, Z. MoS_2 Nanoribbons: High Stability and Unusual Electronic and Magnetic Properties. *J. Am. Chem. Soc.* **2008**, *130*, 16739-16744.

32. Zhao, Y.; Zhang, Z.; Ouyang, G. Lattice Strain Effect on the Band Offset in Single-Layer MoS_2: An Atomic-Bond-Relaxation Approach. *J. Phys. Chem. C* **2017**, *121*, 5366-5371.

33. Vallittu, P. K. Acrylic Resin-fiber Composite - Part II: The Effect of Polymerization Shrinkage of Polymethyl Methacrylate Applied to Fiber Roving on Transverse Strength. *J. Prosthet. Dent.* **1994**, *71*, 613-617.

34. Haugstad, G., *Atomic Force Microscopy: Understanding Basic Modes and Advanced Applications*. John Wiley & Sons: Hoboken, NJ, 2012.

35. Cremons, D. R.; Plemmons, D. A.; Flannigan, D. J. Femtosecond Electron Imaging of Defect-Modulated Phonon Dynamics. *Nat. Commun.* **2016**, *7*, 11230.

36. McKenna, A. J.; Eliason, J. K.; Flannigan, D. J. Spatiotemporal Evolution of Coherent Elastic Strain Waves in a Single MoS_2 Flake. *Nano Lett.* **2017**, *17*, 3952-3958.

37. Zhang, Y.; Flannigan, D. J. Observation of Anisotropic Strain-Wave Dynamics and Few-Layer Dephasing in MoS_2 with Ultrafast Electron Microscopy. *Nano Lett.* **2019**, *19*, 8216-8224.

38. Plimpton, S. Fast Parallel Algorithms for Short-Range Molecular Dynamics. *J. Comput. Phys.* **1995**, *117*, 1-19.

39. Dadgar, A. M.; Scullion, D.; Kang, K.; Esposito, D.; Yang, E. H.; Herman, I. P.; Pimenta, M. A.; Santos, E. J. G.; Pasupathy, A. N. Strain Engineering and Raman Spectroscopy of Monolayer Transition Metal Dichalcogenides. *Chem. Mater.* **2018**, *30*, 5148-5155.

40. Liang, T.; Phillpot, S. R.; Sinnott, S. B. Parametrization of a Reactive Many-Body Potential for Mo-S Systems. *Phys. Rev. B* **2009**, *79*, 245110.

41. Stewart, J. A.; Spearot, D. E. Atomistic Simulations of Nanoindentation on the Basal Plane of Crystalline Molybdenum Disulfide (MoS_2). *Modell. Simul. Mater. Sci. Eng.* **2013**, *21*, 045003.

42. Guénolé, J.; Nöhring, W. G.; Vaid, A.; Houllé, F.; Xie, Z.; Prakash, A.; Bitzek, E. Assessment and Optimization of the Fast Inertial Relaxation Engine (FIRE) for Energy Minimization in Atomistic Simulations and Its Implementation in LAMMPS. *Comput. Mater. Sci.* **2020**, *175*, 109584.